Nanoscale

ROYAL SOCIETY OF CHEMISTRY

PAPER

View Article Online
View Journal | View Issue



Cite this: *Nanoscale*, 2022, **14**, 18115

# Deciphering the photophysical properties of near-infrared quantum emitters in AlGaN films by transition dynamics

Yingxian Xue,†[a] Junxiao Yuan,†[b,c] Qian Li,*[b] Feiliang Chen,*[d] Xinrui Yuan,[a] Zhiping Ju,[a] Shiyu Zhang,[a] Botao Wu,[a] Yidong Hou,[c] Mo Li,[d] Jian Zhang[d] and E Wu *[a,e,f]

Received 9th September 2022,
Accepted 23rd November 2022

DOI: 10.1039/d2nr04978c

rsc.li/nanoscale

Point defects in wide bandgap III-nitride semiconductors have been recently reported to be one kind of the most promising near-infrared (NIR) quantum emitters operating at room temperature (RT). But the identification of the point defect species and the energy level structures as well as the transition dynamics remain unclear. Here, the photophysical properties of single-photon emission from point defects in AlGaN films are investigated in detail. According to the first-principles calculations, a three-level model was established to explain the transition dynamics of the quantum emitters. An anti-site nitrogen vacancy complex ($V_NN_{Ga}$) was demonstrated to be the most likely origin of the measured emitter since the calculated zero-phonon line (ZPL) and the lifetime of $V_NN_{Ga}$ in the AlGaN film coincide well with the experimental results. Our results provide new insights into the optical properties and energy level structures of quantum emission from point defects in AlGaN films at RT and establish the foundation for future AlGaN-based on-chip quantum technologies.



## 1. Introduction

III-Nitrides, consisting of AlN, GaN, InN and their alloys, are the key materials of third-generation semiconductors and have already been commercially used in blue and white light-emitting diodes (LEDs) for many years. Compared with the previous generation semiconductors represented by GaAs, III-nitrides have higher breakdown field strength, larger bandgap and higher electron mobility, which are suitable for applications such as high frequency, high pressure, high power, high temperature and intense irradiation.[1–3] Therefore, III-nitrides play an important role in optoelectronic devices and are the key materials for the development of microelectronics, optoelectronics, power electronics, and so on.[4–11] In particular, the tunable direct bandgap, polarization characteristics, biocompatibility and other superior optical and electronic properties of III-nitrides make them useful for photonic integrated circuit platforms.[12–14] In addition, isolated transition metals (TMs) doped with AlN and GaN appear to represent novel materials that show metamagnetism and possible photo-induced spin crossovers.[15,16]

III-Nitrides do not exist in nature, and the invention of this family of semiconductors to emit light in such a wide range of important wavelengths is a major breakthrough in materials science. The main growth methods for III-nitrides include both metal organic chemical vapor deposition (MOCVD) and molecular beam epitaxy (MBE), and point defects are the cause of defect formation during the growth of AlN, GaN, InN and their alloy films. Point defects in III-nitride semiconductors bind electrons to an exceedingly localized region in the Å scale and show abundant spin and optical properties that can be exploited for the fabrication of quantum devices.[17–21] In addition, the large bandgap can suppress the coupling between the bandgap level and the bulk state, which meets the host material criteria for addressable quantum emitters. Based on the first principles calculation of density functional theory, it was found that only the electrically neutral cation vacancies in the III-nitrides with wide bandgap satisfy a unique Td symmetrical "5-electron-8-orbit" configuration suitable for achieving a fully spin-polarized single-photon emis-

[a]*State Key Laboratory of Precision Spectroscopy, East China Normal University, Shanghai 200241, China. E-mail: ewu@phy.ecnu.edu.cn*
[b]*Microsystem and Terahertz Research Center, China Academy of Engineering Physics, Chengdu, 610299, China. E-mail: liqian612@163.com*
[c]*College of Physics, Sichuan University, Chengdu, Sichuan 610065, China*
[d]*School of Electronics Science and Engineering, University of Electronic Science and Technology of China, Chengdu 610054, China. E-mail: flchen@uestc.edu.cn*
[e]*Chongqing Key Laboratory of Precision Optics, Chongqing Institute of East China Normal University, Chongqing 401120, China*
[f]*Collaborative Innovation Center of Extreme Optics, Shanxi University, Taiyuan, Shanxi 030006, China*
†Co-first authors.

sion.[22] Therefore, the electrically neutral cationic vacancies of wide band III-nitrides are a promising quantum emitter in the field of quantum information.

To date, numerous stable quantum emitters at RT in GaN and AlN films have been reported.[23–29] Single-photon emission from point defects in GaN and AlN films exhibits narrow and strong luminescence with the peak spectrum varying from the visible region (543 nm) to the near-infrared (NIR) (1340 nm) region.[24–26,29] The origin of the quantum emitters is investigated by first-principles calculations, and some of the NIR quantum emitters originate from the antisite nitrogen vacancy complexes ($N_{Al}V_N$) and divacancy complexes ($V_{Al}V_N$).[23] As a ternary compound semiconductor, AlGaN's lattice constant and bandgap are determined by the Al composition and obey Vegard's theorem.[30] The lattice constant is between GaN and AlN, and the bandgap increases with the increase in the Al component and is continuously adjustable from 3.39 eV to 6.2 eV.[31] Therefore, AlGaN can generate a wider variety of point defects than binary compounds such as GaN and AlN, thereby rendering wide-bandgap III-nitrides with defect correlation as a flexible and scalable material platform for quantum emitters.

Defect-related single-photon emission in AlGaN films has been reported in our previous work.[32] The quantum emitter of a single defect in an AlGaN film is bright, linearly polarized and can emit light from 720 nm to 930 nm in the near-infrared spectral range at RT. These advantages make single-point defects in AlGaN films attractive for a variety of applications, especially, quantum information. However, much more work needs to be done to improve the understanding of the photophysics of quantum emitters in AlGaN films. In particular, before these emitters can be used to perform advanced quantum optics experiments, it is important to understand their transition dynamics and level structures at RT.

In this work, we speculated the photophysical properties of stable quantum emission in AlGaN films at RT. The possible point defect types and the transition dynamic behaviors were calculated and analyzed using density functional theory (DFT). The transition kinetics of the optically stable quantum emitter from the defects in AlGaN films at RT was analyzed in detail with a three-level model. Quantum emission and metastable state shelving were observed from the power-dependent measurements using a Hanbury Brown and Twiss (HBT) configuration. We found that the anti-site nitrogen vacancy complex ($V_NN_{Ga}$) has several key physical properties matching those of the experimentally observed quantum emitter. These include the zero-phonon line, photoluminescence lifetime, and photoluminescence spectrum. The identification of defect candidates for $V_NN_{Ga}$ emission paves the way for controllable quantum emission generation.

## 2. Results and discussion

### 2.1 Theoretical calculations

First-principles calculations were performed to theoretically identify the types and the energy level structures of the point defects as well as the transition dynamics in AlGaN films. We systematically calculated and analyzed several kinds of possible intrinsic defects in $Al_{0.25}Ga_{0.75}N$, including single-vacancy ($V_{Ga}$, $V_{Al}$, and $V_N$), interstitial atoms ($Ga_i$, $N_i$, and $Al_i$), di-vacancy ($V_NV_N$, $V_NV_{Ga}$, $V_NV_{Al}$, and $V_{Al}V_{Ga}$), anti-site complex ($Ga_NN_{Ga}$, $Ga_{Al}Al_{Ga}$, and $Al_NN_{Al}$), anti-site nitrogen vacancy complex ($V_NN_{Ga}$ and $V_NN_{Al}$) and so on. Among these defects, $V_NN_{Ga}$ is found to be one of the most likely origins of the measured emitter in AlGaN films. The host materials used in the experiment are $Al_{0.2}Ga_{0.8}N$ (400 nm)/$Al_{0.3}Ga_{0.7}N$ (400 nm), and it has been demonstrated that a small difference in the constituents of AlGaN has a limited impact on the ZPL and the lifetime of point defects.[22] Therefore, we used $Al_{0.25}Ga_{0.75}N$ for the first-principles calculations for simplicity because it was much easier to construct a stable supercell structure. The first-principles calculations based on the DFT were performed using the PWmat package.[33,34] The atomic positions were optimized using the Perdew–Burke–Ernzerhof (PBE) function and the self-consistent field (SCF) calculations were performed using the Heyd–Scuseria–Ernzerhof (HSE) hybrid function. Fig. 1(a) presents the atomic structure of the $V_NN_{Ga}$ defect in $Al_{0.25}Ga_{0.75}N$. The complex defect is built by putting an anti-site nitrogen ($N_{Ga}$) in a nitrogen vacancy's ($V_N$) nearest neighbor position.[35] The bulk structure of $Al_{0.25}Ga_{0.75}$ is a typical Wurtzite structure, which is built *via* an improved cluster expansion (CE) method to reduce errors.[36] A supercell containing 3 × 3 × 2 primitive cells was used for defect calculations. All calculations are spin-polarized, and the energy cutoff of the SCFs is set to 50 Ry (Rydberg).

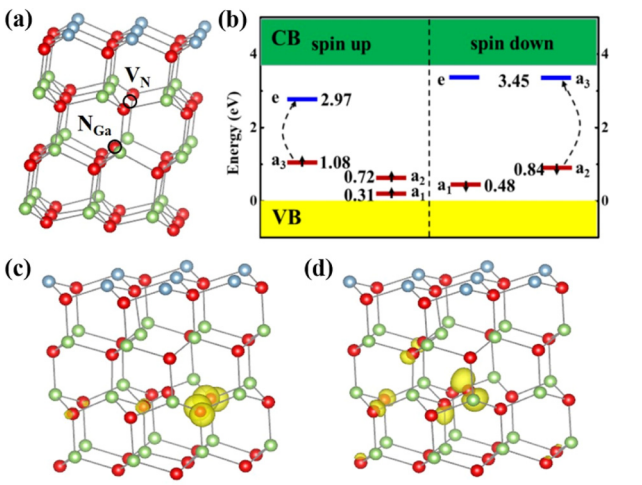


**Fig. 1** (a) Atomic structure of the $V_NN_{Ga}$ defect in $Al_{0.25}Ga_{0.75}N$. The red, green and blue balls represent the nitrogen, gallium and aluminum atoms, respectively. (b) Defect-level diagrams of $V_NN_{Ga}$ in $Al_{0.25}Ga_{0.75}N$. The solid arrow represents the spin direction and the dotted arrow represents the transition in spin-up channel that exists from the *e* to $a_3$ and the transition in the spin-down channel exists from $a_3$ to $a_2$ (or *e* and $a_2$). (c) The isosurface of the molecular orbital corresponding to the defect level with $a_2$ (spin down). (d) The isosurface of the molecular orbital corresponding to the defect level with *e* (spin down).

Fig. 1(b) shows the calculated Kohn–Sham single particle defect level of the defect pair $V_NN_{Ga}$ at the ground state. The defect brings in four different energy levels for both the spin-up and spin-down electrons between the valence band maximum (VBM) and the conduction band minimum (CBM), *i.e.* $a_1$, $a_2$, $a_3$ and $e$. The spin-up and spin-down levels split apart and the electron-occupied $a_2$ (spin down) and $a_3$ (spin up) levels are located at about 1 eV above the VBM, avoiding interference from the optical transition introduced by the electronic states of the host material. This is an essential condition for achieving quantum emission with point defects. The ground state configuration is identified as $a_1^2a_2^2a_3$ according to the Pauli exclusion principle and Hund's rules. The $a_1^2a_2a_3^2$ and $a_1^2a_2a_3e$ are two electronic configurations that cause the electron transition in the spin-down channel (from $a_2$ to $a_3$) and the spin-up channel (from $a_3$ to $e$) respectively. The $a_1^2a_2^2a_3$, $a_1^2a_2a_3^2$ and $a_1^2a_2a_3e$ are represented by state 1, state 2 and state 3 for the convenience of further discussion. To verify the origin of the defect levels, we calculated the isosurface of the defect levels in the state 1 spin-down channel. Fig. 1(b) and (c) show the isosurface of the defect levels, corresponding to $e$ and $a_3$ in the defect-level diagrams as shown in Fig. 1(d). The charge density of the molecular orbital shows the characteristics of high localization. Most of the charge density for $a_3$ is provided by the three nearest neighbors of $N_{Ga}$, and in the meantime, the $N_{Ga}$ provides most of the charge density for $e$.

Fig. 2(a) shows the schematic configuration coordinate diagrams of the defect-pair $V_NN_{Ga}$ in AlGaN which show the defect-dependent photophysical processes. The calculated results indicate that the lowest energy of metastable state 3 is higher than that of ground state 1 and the bottom of excited state 2 is the highest among the three. The calculated ZPL and ZPL values corresponding to the energy of ZPL from metastable state 3 and excited state 2 to ground state 1 are 1.04 eV (1170 nm) and 1.46 eV (849 nm), respectively. The calculated ZPL value and the experimental value of 1.41 eV (874 nm)[32] are in excellent agreement and the deviation is less than 0.05 eV. This deviation may be attributed to the structural strains and the small component difference as well as the "unphysical" spreading of the polarization charge and the presence of the neutralizing background, and it would decrease as the size of the supercell increases. The strain has been proved to have a strong effect on ZPL wavelength. For example, the calculated results show that the strain could modulate the ZPL emission wavelength of point defects in GaN and AlN obviously (from 1.49 eV to 0.7 eV corresponding to 5% compressive strain) as reported by ref. 22. The PA (photon absorption) is 1.90 eV, which also matches the experimental energy of excitation light of 1.87 eV (662 nm). Thus, we believe that the transition for spin-down has a high probability of being the origin of the measured single quantum emitter in the experiment.

To better understand the transition process between the quantum states of the $V_NN_{Ga}$ in AlGaN film, the schematic of the three-energy model and the intrinsic dynamics is given in Fig. 2(b), in which $r_{ij}$ represents the transition rate from State $i$ to State $j$. If $r_{ij}$ represents an energy-releasing process such as $r_{21}$, $r_{31}$, and $r_{23}$, then it could be simply obtained by $r_{ij} = W_{rad}(\omega)_{ij}$, which is the radioactive rate. Conversely, when $r_{ij}$ represents a process with absorption of energy such as $r_{12}$, $r_{13}$, and $r_{32}$, then $r_{ij}$ is usually not a constant but varies according to the formation of the excitation energy. For example, when excited by a laser, $r_{12}$ should relate to the laser power and the photon energy. Considering the influence of the thermal activation energy and the detailed temperature dependence of the photoluminescence (PL) balance,[36] $r_{13}$ and $r_{32}$ can be obtained by $r_{ij} = W_{rad}(\omega)_{ij} \times \exp(-\Delta E_{ij}/kT)$, where $\Delta E_{ij}$ is the energy difference between state $i$ and state $j$, $k$ is the Boltzmann constant, and $T$ is the temperature. The radioactive rate $W_{rad}(\omega)_{ij}$ is governed by Fermi's golden rule as

$$W_{rad}(\omega)_{ij} = \frac{\omega^3 n \left|\mu_{ij}\right|^2}{3\pi\varepsilon_0 \hbar c^3}, \quad (1)$$

where $\hbar$ is the reduced Planck constant, $\omega$ is the frequency of the emitted photon, $|\mu_{ij}|$ is the transition dipole moment, $n$ is the refraction index, $\varepsilon_0$ is the vacuum permittivity, and c is the

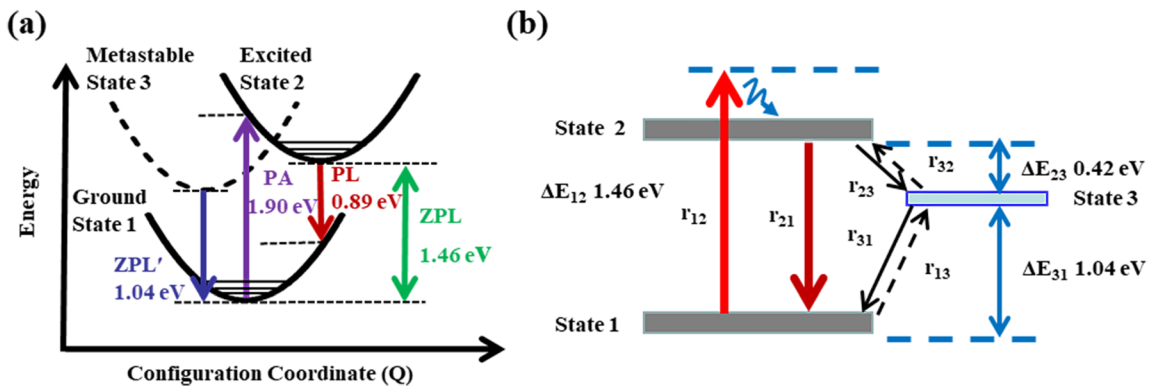


**Fig. 2** (a) Configuration coordinate diagram of the transition process between $e$ and $a_3$ with spin-down. (b) Model of the intrinsic dynamics of $V_NN_{Ga}$. Dashed lines represent low transition probability and solid lines represent high transition probability. The wave line represents structural relaxation.

speed of light in vacuum, respectively. Moreover, the radioactive lifetime $\tau$ is the inverse of $W_{rad}(\omega)$ by $\tau = 1/W_{rad}$.

The single photon emission property of the $V_NN_{Ga}$, including transition rate $r_{ij}$, lifetime $\tau$ and the ZPL are quantitatively calculated and listed in Table 1. The ZPL lies within the optimal range for low-loss fiber transmission. Moreover, the calculated radiative lifetime $\tau$ of $V_NN_{Ga}$ is comparable with that of the $SiV^-$ center in diamonds, which makes this type of quantum emitter especially promising for applications in quantum technology.

### 2.2 Experiments and discussion

The AlGaN film used in the experiment was prepared using metal organic chemical vapor deposition (MOCVD), first growing a 25 nm-thick AlN buffer layer film on 2-inch sapphire substrates and then growing a 400 nm-thick $Al_{0.2}Ga_{0.8}N$ layer and a 400 nm-thick $Al_{0.3}Ga_{0.7}N$ layer film. A low temperature AlN buffer and a low Al-content $Al_{0.2}Ga_{0.8}N$ buffer are employed to control and compensate for the growth stress and suppression of crack formation during the subsequent growth of high Al-content $Al_{0.3}Ga_{0.7}N$. Therefore, the two different Al-content AlGaN films are actually used to obtain high Al-content AlGaN films with good crystalline quality. Fig. 3(a) shows the surface morphology of the AlGaN film by atomic force microscopy (AFM). The obtained AFM image shows that the surface of the AlGaN film was homogeneous and flat, revealing the high crystal quality of the AlGaN film. Experiments were performed to verify the proposed theoretical calculations, using a scanning confocal microscope with a Hanbury Brown–Twiss (HBT) setup to study the fluorescence characteristics of the point defects in the AlGaN film at RT. A laser beam of 662 nm was focused on the AlGaN film by an oil-immersion objective (100×, N.A. = 1.3, Olympus) to generate the fluorescence from the single-point defects in the AlGaN film. A more detailed description of the technique can be found in our previous work in ref. 32. The quantum emitters of point defects in the AlGaN film are randomly distributed in the spectral range from 720 nm to 930 nm. Different emitters of the point defects in the AlGaN film show different distinct emission lines but the linewidths of all single emitters are less than 10 nm. We estimated the depth of the point defects from the surface of the AlGaN film according to the microscope $z$-axis scan image.[37] Fig. 3(b) shows a 10 × 10 μm$^2$ $X$–$Z$ plane fluorescence scan image containing the quantum emitters. The $z$-axis indicates the scan depth. The surface of the AlGaN film is calibrated as $Z = 0$ and the green dashed line indicates the surface of the AlGaN film according to the excitation light reflection distribution along the $z$-axis as shown in the inset of Fig. 3(b). Below the green dotted line, there is the immersion oil for the microscope objective above the surface of the AlGaN film. The fluorescence intensity inside the film is a little higher than that outside due to the background noise from the yellow luminescence (YL) inside the AlGaN film. It is generally believed that the YL is caused by the transition from the conduction band or a shallow donor to the deep energy level and should be related to structural defects.[32] The $z$-axis in Fig. 3(b)

**Table 1** Calculated results of the photophysical parameters of the single emitter in the AlGaN film

| | $\Delta E$ | Transition rates ($r$) | Lifetime ($\tau$) |
|---|---|---|---|
| Between state 2 and state 1 | 1.46 eV (849 nm) | $r_{21} = 0.2\ ns^{-1}$ | 5.00 ns |
| Between state 3 and state 1 | 1.04 eV (1170 nm) | $r_{31} = 5.17 \times 10^{-4}\ ns^{-1}$, $r_{13} = 2.2 \times 10^{-21}\ ns^{-1}$ | $1.93 \times 10^3$ ns |
| Between state 2 and state 3 | 0.42 eV (2953 nm) | $r_{32} \ll r_{23}$ | — |

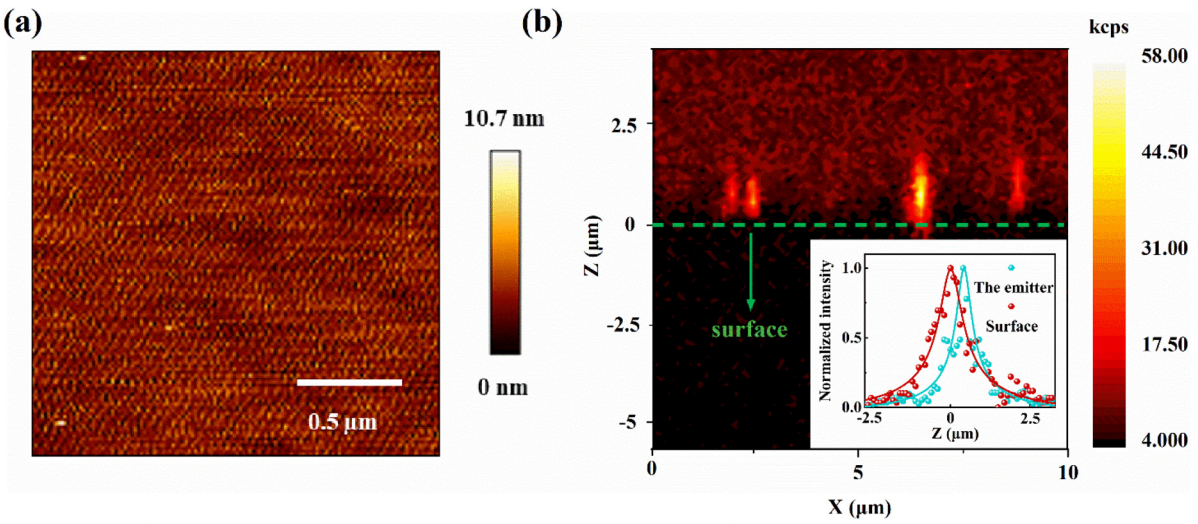


**Fig. 3** (a) A typical 2 × 2 μm$^2$ AFM image of the AlGaN film. (b) $X$–$Z$ plane confocal fluorescence scanning image of quantum emitters in the AlGaN film with a scanning range of 10 × 10 μm$^2$. The surface of the AlGaN film is calibrated as $Z = 0$ and the green dotted line represents the surface of the AlGaN film. Inset: the AlGaN film surface reflection excitation light intensity and the PL intensity of a single quantum emitter along the $Z$-axis.

corresponds to the absolute *z*-axis piezo position of the scanner. The difference between the two curves shown in the inset of Fig. 3(b) indicates the depth of the emitter. Therefore, the AlGaN film surface and the quantum emitter are located at 2.66 μm and 3.11 μm, respectively. So the depth of the emitter from the surface is about 450 nm. In addition, we also estimated the depth of several other different point defects from the surface of the AlGaN film. Most of the point defects are randomly distributed about 400 nm below the sample surface and near the interface of the $Al_{0.2}Ga_{0.8}N$ layer and the $Al_{0.3}Ga_{0.7}N$ layer. As explained in the previous reports,[38,39] the point defects might reside inside or next to a stacking fault and the density of the point defects is positively correlated with the threading dislocations and stacking faults. Much more threading dislocations and stacking faults usually appear near the AlGaN/AlGaN interface, so it is reasonable that most of the point defects were close to the AlGaN/AlGaN interface but not inside the AlGaN film. However, further studies are needed to draw such a conclusion. A systematic contrastive study should be done if we can obtain single AlGaN films with good crystalline quality.

To further clarify the consistency between the measured quantum emitter in the experiment and $V_NN_{Ga}$, a three-level system composed of the ground state $|1\rangle$, the excited state $|2\rangle$ and the metastable state $|3\rangle$ was modelled. These states are coupled by the transition rate coefficient $r'_{ij}$, where $r'_{ij}$ (with $i$, $j$ = 1, 2, and 3) indicates the transition rate from level $|i\rangle$ to level $|j\rangle$.[40] During photon absorption, the ground state $|1\rangle$ is coupled with the excitation rate coefficient $r'_{12}$ to the excited state $|2\rangle$. In the case of a two-level transition, excited particles returning from the excited state $|2\rangle$ to the ground state $|1\rangle$ result in photon emission with a radiative decay coefficient $r'_{21}$. In the three-level system, no photon emission occurs when the excited particles go from the metastable state $|3\rangle$ to the ground state $|1\rangle$ *via* a nonradiative decay coefficient $r'_{31}$. The relaxation rate $r'_{23}$ is a nonradiative channel in which no photon is emitted as long as the particle remains in a metastable state. Therefore, optical transition systems involving at least one metastable state should show power dependence.

In the previous work, the antibunching fit parameter $\lambda_1$ is obtained,[32] and $\lambda_1 = r'_{12} + r'_{21}$. By linearly fitting $\lambda_1$ as a function of the excitation power, we can get the values of $r'_{12}$ and $r'_{21}$; $r'_{21}$ = 0.36 ns$^{-1}$, and $\tau$ = 2.7 ns. On the long timescale ($\tau \geq$ 30 ns), the $g^{(2)}(\tau)$ function was unperturbed by the bunching associated with the photoluminescence of the single emitter. The experimental data can be fit optimally according to[41,42]

$$g^{(2)}(\tau) = 1 + \alpha e^{-\lambda_2|\tau|}, \quad (2)$$

$$\lambda_2 = r'_{31} + r'_{23}r'_{12}/(r'_{12} + r'_{21}), \quad (3)$$

where $\lambda_2$ is the bunching fit parameter. The value of $g^{(2)}(\tau)$ is always larger than that on the long timescale, corresponding to the bunching effect caused by leakage into the metastable level of the three-level model. Fig. 4(a) shows the power-dependent second-order autocorrelation functions for this emitter at RT on a long timescale with different colors for different excitation powers. The red solid lines are fittings according to eqn (2). The bunching fit parameter $\lambda_2$ is obtained by fitting $g^{(2)}(\tau)$ on the long timescale at different excitation powers. In addition, $\lambda_2$ as a function of the excitation power can be fitted as shown in Fig. 4(b) according to eqn (3), which can be used to represent the metastable behavior. We have $r'_{23} = 1.3 \times 10^{-3}$ ns$^{-1}$ and $r'_{31} = 2.19 \times 10^{-4}$ ns$^{-1}$. It is shown that the quantum emitter associated with the point defect increases the population of the metastable state (a non-radiative process) at a high excitation power, corroborating the involvement of the metastable state in the transition kinetics at RT.

For three-level systems, the power-dependent emission count rate reaches saturation as shown in Fig. 4(c). With both $r'_{12}$ and $r'_{21}$ deduced from the short timescale measurements, the detected fluorescence intensity at different excitation powers can be fitted according to

$$R = \eta_{det}\eta_Q \frac{r'_{21}}{\left(\frac{r'_{21}}{r'_{12}} + \frac{r'_{23}}{r'_{31}} + 1\right)}, \quad (4)$$

where $R$ is the total count rate of the emitter and $\eta_{det}$ and $\eta_Q$ imply the detection efficiency of the whole confocal microscope system and the photoluminescence quantum efficiency, respectively. Taking the values of $r'_{12}$, $r'_{21}$, $r'_{23}$, $r'_{31}$ and $R$ into eqn (4), $\eta_{det} \times \eta_Q = 3.43 \times 10^{-3}$ is obtained for this emitter. The detection efficiency of our set-up includes the collection efficiency of the microscope objective with NA = 1.3 working with immersion oil $\eta_{col} \approx 7\%$, sphericity aberration $\eta_{ab} \approx 80\%$, objective transmittance $\eta_{trans} \approx 76.1\%$, optical transmittance $\eta_{opt} \approx 30\%$, and quantum efficiency of silicon avalanche photodiodes $\eta_{APD} \approx 46.5\%$ at the wavelength of the measured emitter. The estimated detection efficiency is the product of $\eta_{col}$, $\eta_{ab}$, $\eta_{trans}$, $\eta_{opt}$ and $\eta_{APD}$ with a value of approximately $5.9 \times 10^{-3}$. The main limit of $\eta_{det}$ lies in the collection efficiency of the microscope objective. Notably, a number of structures are studied to enhance the collection efficiency by an objective lens with limited NA, such as suitable passivation, integration of the single emitters in cavities, plasmonic structures and more.[43–46] The photoluminescence quantum efficiency $\eta_Q$ is roughly estimated to be about 57%.

The theoretically calculated transition rate $r_{ij}$ and lifetime $\tau$, as listed in Table 1, were compared with the experimental results. The theoretically calculated $r_{21}$ is 0.2 ns$^{-1}$, corresponding to $\tau$ = 5.0 ns, which matches with the experimental result of 0.37 ns$^{-1}$ upon transition from the excited state to the ground state. Therefore, we can infer that state 2 in the theoretical calculation is the estimated excited state $|2\rangle$ in the experiment. Similarly, $r_{31}$ is calculated to be $5.17 \times 10^{-4}$ ns$^{-1}$, which matches with the transition rate from the metastable state to the ground state $r'_{31} = 2.19 \times 10^{-4}$ ns$^{-1}$, indicating that the theoretically calculated state 3 is the metastable state $|3\rangle$. The transition energy $\Delta E_{23}$ = 0.42 eV is relatively quite high compared to the thermal energy $kT$ = 0.026 eV ($T$ = 300 K) at RT; therefore, it is clear that $r_{32}$ is much less than $r_{23}$ according to $r_{32} = r_{23}\exp(-\Delta E_{23}/kT)$. It can be concluded that the metastable state could not be spontaneously transformed into the

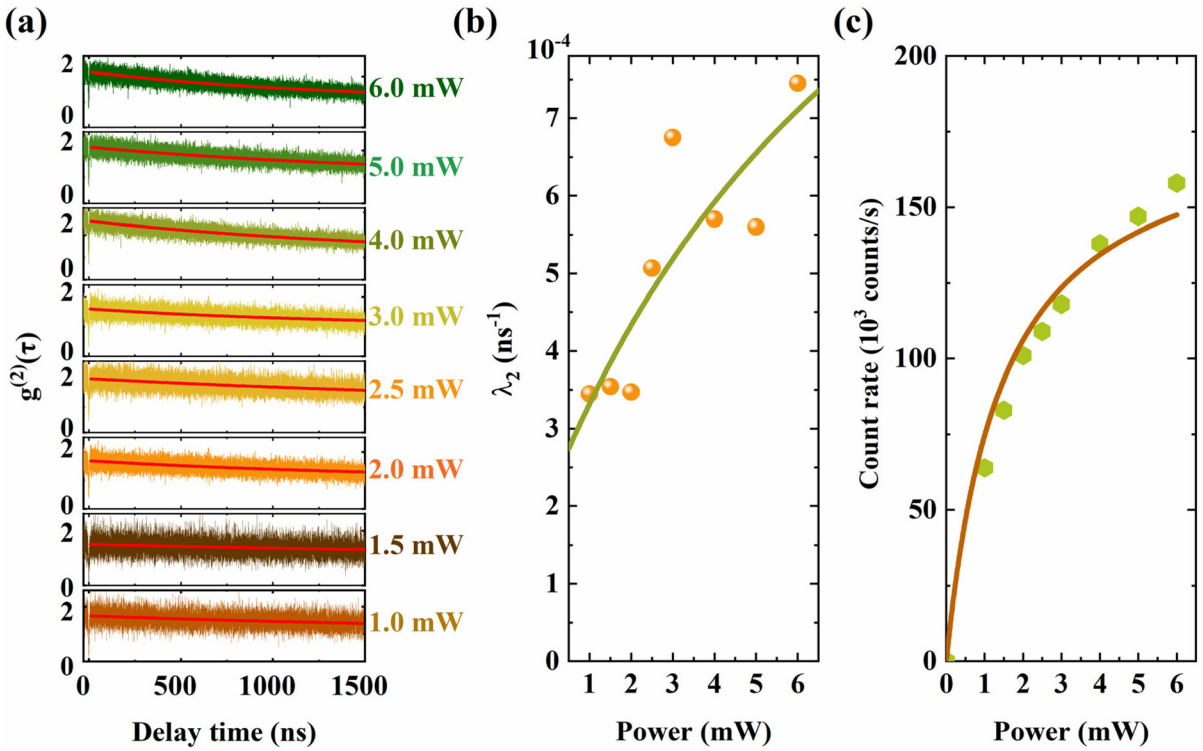


Fig. 4 (a) Second-order autocorrelation function at different excitation powers over long time scales. Different colors represent experimental data under different excitation powers, while the red lines are the best fit obtained with three-level second-order autocorrelation functions of eqn (4). (b) Power dependence of $\lambda_2$ (orange dots) with fitting (green line). (c) Excitation-power-dependent emission count rate. The green hexagons represent the total counting rate by APD1 and APD2, while the brown curve represents the fitting according to eqn (4).

excited state without absorbing external energy, such as phonon energy. The same conclusion can be drawn for the transition between the ground state and the metastable state because of $\Delta E_{31}$ = 1.04 eV. The above conclusions show that the theoretically calculated state 3 is the metastable state $|3\rangle$ rather than the excited state $|2\rangle$. As a result, the calculated ZPL and the lifetime of $V_NN_{Ga}$ referring to the transition from the occupied $a_2$ (in spin down channel) to the unoccupied $a_3$ level is a possible origin of the photoluminescence observed in the experiment, and the transition from the occupied $a_3$ (in spin up channel) to the unoccupied $e$ level may be responsible for the metastable state $|3\rangle$ in the experiment. In addition, the wavelength of the point defect measured in our experiment has a small deviation from the calculated wavelength value of ZPL. This deviation can be attributed to lattice deformation caused by the internal stress when AlGaN is actually grown.

## 3. Conclusions

In summary, we have investigated in detail the key photophysical properties of a NIR quantum emitter from single-point defects in AlGaN films both theoretically and experimentally, including ZPL, PL lifetime and PL spectra. We demonstrate the consideration of the key photoluminescence parameters and transition kinetics in defect identification through theoretical and experimental comparison. All the relevant properties of $V_NN_{Ga}$ obtained by first principles calculations in AlGaN agree with the experimental results very well, giving a possible origin of the measured emitter. This work provides deeper insights into near infrared quantum emission from both the theoretical and experimental perspectives, which have significant importance in revealing the unknown chemical properties of point defects in AlGaN films and pave the way for the integration of on-chip quantum devices and networks.

## Author contributions

The manuscript was written through the contributions of all authors. All authors have given their approval for the final version of the manuscript.

## Conflicts of interest

There are no conflicts to declare.

## Acknowledgements

This work was supported by the National Key R&D Program (2021YFA1201503), the National Natural Science Foundation of

 

China (no. 61704162, 61704163, 61875178, U1380109 and 11621404), the Natural Science Foundation of Shanghai (22ZR1421100), the Science Challenging Project (no. TZ2016003), the Fundamental Research Funds for the Central Universities, the Natural Science Foundation Project of CQ (CSTC2021JCYJ-MAXMX0356) and the Research Funds of Happiness Flower ECNU (2021ST2110).

## Notes and references

1 K. J. Chen, O. Häberlen, A. Lidow, C. Tsai, T. Ueda, Y. Uemoto and Y. Wu, *IEEE Trans. Electron Devices*, 2017, **64**, 779–795.
2 J. Ben, X. Liu, C. Wang, Y. Zhang, Z. Shi, Y. Jia, S. Zhang, H. Zhang, W. Yu, D. Li and X. Sun, *Adv. Mater.*, 2021, **33**, 2006761.
3 C. Bayram, N. Pere-laperne, R. McClintock, B. Fain and M. Razeghi, *Appl. Phys. Lett.*, 2009, **94**, 121902.
4 Y. C. Sim, S. H. Lim, Y. S. Yoo, M. H. Jang, S. Choi, H. S. Yeo, K. Y. Woo, S. Lee, H. G. Song and Y. H. Cho, *Nanoscale*, 2018, **10**, 4686–4695.
5 M. Kneissl, T. Y. Seong, J. Han and H. Amano, *Nat. Photonics*, 2019, **13**, 233–244.
6 C. Huang, H. Zhang and H. Sun, *Nano Energy*, 2020, **77**, 105149.
7 S. Zhou, X. Zhao, P. Du, Z. Zhang, X. Liu, S. Liu and L. J. Guo, *Nanoscale*, 2022, **14**, 4887–4907.
8 M. Feng, J. Liu, Q. Sun and H. Yang, *Prog. Quantum Electron.*, 2021, **77**, 100323.
9 S. Arafin, X. Liu and Z. Mi, *J. Nanophotonics*, 2013, **7**, 074599.
10 F. F. Sudradjat, W. Zhang, J. Woodward, H. Durmaz, T. D. Moustakas and R. Paiella, *Appl. Phys. Lett.*, 2012, **100**, 241113.
11 F. Giannazzo, G. Fisichella, G. Greco, A. La Magna, F. Roccaforte, B. Pecz, R. Yakimova, R. Dagher, A. Michon and Y. Cordier, *Phys. Status Solidi A*, 2017, **214**, 1600460.
12 H. Matsubara, S. Yoshimoto, H. Saito, Y. Jianglin, Y. Tanaka and S. Noda, *Science*, 2008, **319**, 445.
13 T. Tawara, H. Gotoh, T. Akasaka, N. Kobayashi and T. Saitoh, *Phys. Rev. Lett.*, 2004, **92**, 256402.
14 M. Arita, S. Kako, S. Iwamoto and Y. Arakawa, *Appl. Phys. Express*, 2012, **5**, 126502.
15 X. Y. Cui, B. Delley, A. J. Freeman and C. Stampfl, *Phys. Rev. Lett.*, 2006, **97**, 016402.
16 H. K. Seong, J. Y. Kim, J. J. Kim, S. C. Lee, S. R. Kim, U. Kim, T. Park and H. J. Choi, *Nano Lett.*, 2007, **7**, 3366–3371.
17 R. Hanson and D. D. Awschalom, *Nature*, 2008, **453**, 1043–1049.
18 V. Scarani, H. Bechmann-Pasquinucci, N. J. Cerf, M. Dušek, N. Lütkenhaus and M. Peev, *Rev. Mod. Phys.*, 2009, **81**, 1301–1350.
19 H. K. Lo, M. Curty and K. Tamaki, *Nat. Photonics*, 2014, **8**, 595–604.
20 P. Kok, W. J. Munro, K. Nemoto, T. C. Ralph, J. P. Dowling and G. J. Milburn, *Rev. Mod. Phys.*, 2007, **79**, 135–174.
21 M. Gimeno-Segovia, P. Shadbolt, D. E. Browne and T. Rudolph, *Phys. Rev. Lett.*, 2015, **115**, 020502.
22 H. Zang, X. Sun, K. Jiang, Y. Chen, S. Zhang, J. Ben, Y. Jia, T. Wu, Z. Ahi and D. Li, *Adv. Sci.*, 2021, **8**, 2100100.
23 Y. Xue, H. Wang, N. Xie, Q. Yang, F. Xu, B. Shen, J. J. Shi, D. Jiang, X. Dou, T. Yu and B. Q. Sun, *J. Phys. Chem. Lett.*, 2020, **11**, 2689–2694.
24 A. M. Berhane, K. Y. Jeong, C. Bradac, M. Walsh, D. Englund, M. Toth and I. Aharonovich, *Phys. Rev. B*, 2018, **97**, 165202.
25 Y. Zhou, Z. Wang, A. Rasmita, S. Kim, A. Berhane, Z. Bodrog, G. Adamo, A. Gali, I. Aharonovich and W. B. Gao, *Sci. Adv.*, 2018, **4**, eaar3580.
26 Y. Xue, T. Wei, H. Chang, D. Liang, X. Dou and B. Q. Sun, *J. Phys. Chem. C*, 2021, **125**, 11043–11047.
27 P. C. Bowes, Y. Wu, J. N. Baker, J. S. Harris and D. L. Irving, *Appl. Phys. Lett.*, 2019, **115**, 052101.
28 J. B. Varley, A. Janotti and C. G. Van de Walle, *Phys. Rev. B*, 2016, **93**, 161201.
29 T. J. Lu, B. Lienhard, K. Y. Jeong, H. Moon, A. Iranmanesh, G. Grosso and D. Englund, *ACS Photonics*, 2020, **7**, 2650–2657.
30 R. E. Nahory, M. A. Pollack, W. D. Johnston and R. L. Barns, *Appl. Phys. Lett.*, 1978, **33**, 659–661.
31 Q. Cai, H. You, H. Guo, J. Wang, B. Liu, Z. Xie, D. Chen, H. Lu, Y. Zheng and R. Zhang, *Light: Sci. Appl.*, 2021, **10**, 1–31.
32 Y. Xue, F. Chen, Z. Fang, S. Zhang, Q. Li, M. Li, J. Kang, J. Zhang, S. Shen, B. Wu and E Wu, *Appl. Phys. Lett.*, 2021, **118**, 131103.
33 W. Jia, J. Fu, Z. Cao, L. Wang, X. Chi, W. Gao and L. W. Wang, *J. Comput. Phys.*, 2013, **251**, 102–115.
34 J. Heyd, G. E. Scuseria and M. Ernzerhof, *J. Chem. Phys.*, 2003, **118**, 8207–8215.
35 M. A. Reshchikov and R. Y. Korotkov, *Phys. Rev. B: Condens. Matter Mater. Phys.*, 2001, **64**, 115205.
36 A. Seko, Y. Koyama and I. Tanaka, *Phys. Rev. B: Condens. Matter Mater. Phys.*, 2009, **80**, 165122.
37 A. J. Häußler, P. Heller, L. P. McGuinness, B. Naydenov and F. Jelezko, *Opt. Express*, 2014, **22**, 29986–29995.
38 A. M. Berhane, K. Y. Jeong, Z. Bodrog, S. Fiedler, T. Schröder, N. V. Triviño, T. Palacios, A. Gali, M. Toth, D. Englund and I. Aharonovich, *Adv. Mater.*, 2017, **29**, 1605092.
39 M. Nguyen, T. Zhu, M. Kianinia, F. Massabuau, I. Aharonovich, M. Toth, R. Oliver and C. Bradac, *APL Mater.*, 2019, **7**, 081106.
40 B. Lienhard, T. Schröder, S. Mouradian, F. Dolde, T. T. Tran, I. Aharonovich and D. Englund, *Optica*, 2016, **3**, 768–774.
41 I. Aharonovich, S. Castelletto, D. A. Simpson, A. D. Greentree and S. Prawer, *Phys. Rev. A*, 2010, **81**, 043813.

42 E Wu, V. Jacques, H. Zeng, P. Grangier, F. Treussart and J. F. Roch, *Opt. Express*, 2006, **14**, 1296–1303.
43 F. Lenzini, N. Gruhler, N. Walter and W. H. P. Pernice, *Adv. Quantum Technol.*, 2018, **1**, 1800061.
44 S. Zhang, Y. Liang, Q. Jing, Z. Lu, Y. Lu and T. Xu, *Sci. Rep.*, 2017, **7**, 1–8.
45 S. Xia, T. Aoki, K. Gao, M. Arita, Y. Arakawa and M. J. Holmes, *ACS Photonics*, 2021, **8**, 1656–1661.
46 M. Moczała-Dusanowska, Ł. Dusanowski, O. Iff, T. Huber, S. Kuhn, T. Czyszanowski, C. Schneider and S. Höfling, *ACS Photonics*, 2020, **7**, 3474–3480.